[9] Brodak JW, Kilbourn MR, Welch MJ, Katzenellenbogen JA. Application of robotics to radiopharmaceutical preparation: controlled synthesis of fluorine-18 16α-fluoroestradiol-17β. J Nucl Med 1986;27:714–21.

[10] Lim JL, Zheng L, Berridge MS, Tewson TJ. The use of 3-methoxymethyl-16β,17β-epiestriol-*O*-cyclic sulfone as the precursor in the synthesis of F-18 16α-fluoroestradiol. Nucl Med Biol 1996;23:911–5.

[11] Lim JL, Berridge MS, Tewson TJ. Preparation of [^{18}F]16α-fluoro-17β-estradiol by selective nucleophilic substitution. J Label Compd Radiopharm 1994;35:176–7.

[12] Römer J, Steinbach J, Kasch H. Studies on the synthesis of 16α-[^{18}F]fluoroestradiol. Appl Radiat Isot 1996;47:395–9.

[13] Römer J, Füchtner F, Steinbach J, Johannsen B. Automated production of 16α-[^{18}F]fluoroestradiol for breast cancer imaging. Nucl Med Biol 1999;26:473–9.

資料(7)

資料 7

Available online at www.sciencedirect.com
ScienceDirect
Gynecologic Oncology 104 (2007) 764–766
Gynecologic Oncology
www.elsevier.com/locate/ygyno

Case Report

The positron emission tomography with F18 17β-estradiol has the potential to benefit diagnosis and treatment of endometrial cancer

Yoshio Yoshida [a,*], Tetsuji Kurokawa [a], Yoko Sawamura [a], Akiko Shinagawa [a], Hidehiko Okazawa [b], Yasuhisa Fujibayashi [b], Fumikazu Kotsuji [a]

[a] *Department of Obstetrics and Gynecology, Faculty of Medical Sciences, University of Fukui, Matsuoka-cho, Yoshida-gun, Fukui-ken 910-1193, Japan*
[b] *Biomedical Imaging Research Center, Faculty of Medical Sciences, University of Fukui, Matsuoka-cho, Yoshida-gun, Fukui-ken 910-1193, Japan*

Received 18 July 2006
Available online 6 December 2006

Abstract

Background. The positron emission tomography (PET) with F18 17β-estradiol (FES) has good imaging for assessment of estrogen receptor in breast cancer.

Case. We report on a 30-year-old woman who desired to preserve her fertility with well-differentiated endometrial adenocarcinoma. Before hormone treatment was started, FES-PET showed increased uptake of endometrium, magnetic resonance imaging (MRI) showed thickness and F-18 fluorodeoxyglucose (FDG)-PET showed increased uptake. FES-PET after 3 months showed remaining FES uptake, but there were no abnormal findings on MRI and FDG-PET. Hysteroscopy showed remaining adenocarcinoma. After additional treatment, FES-PET showed a therapeutic response, and hysteroscopy showed no abnormal finding.

Conclusions. To our knowledge, this is the first report that FES-PET has the potential to provide more useful information than did FDG-PET about the hormone therapy.

Keywords: FES-PET; Endometrial cancer; Endocrine treatment

Introduction

Endometrial cancer is the most common gynecological malignancy in North American and European women, and the incidence continues to rise. Mortality from endometrial cancer ranks eighth among cancer deaths in North American women, and in Europe nearly 10,000 women die of this disease each year [1]. For young women (under age 40) who desired to preserve their fertility with well-differentiated endometrial adenocarcinoma, conservative treatment with periodic use of progestin is available [2,3]. Present methods to assess tumor responsiveness require a tissue sample obtained by performing a dilatation and curettage (D & C) every 3 months [3]. Sample availability is thus limited by potential morbidity and sampling problems. A noninvasive method to assess tumor responsiveness would avoid unnecessary diagnostic biopsies of the endometrium and permit serial assessments during treatment.

Positron emission tomography (PET) is a highly sensitive, noninvasive technology that is ideally suited for pre-clinical and clinical imaging of cancer biology, in contrast to anatomical approaches. By using radiolabeled tracers, PET can yield cross-sectional images that reflect tissue biochemistry [4]. Two radiolabeled tracers hold promise for the diagnosis and management of endometrial cancer. The most extensively studied of these is F-18 fluorodeoxyglucose (FDG); the other one is F-18 17β-estradiol (FES) [4]. FES-PET has good imaging characteristics in human studies to predict response to endocrine treatment in breast cancer [5]. But there has been no report published on whether FES-PET provides information useful for assessing tumor response to systemic therapy, or whether FES-PET provides more useful information than FDG-PET in endometrial cancer.

Case

We report on an unmarried 30-year-old woman who presented with well-differentiated adenocarcinoma (Fig. 1A)

* Corresponding author. Fax: +81 776 61 8117.
E-mail address: yyoshida@fmsrsa.fukui-med.ac.jp (Y. Yoshida).

0090-8258/$ - see front matter © 2006 Elsevier Inc. All rights reserved.
doi:10.1016/j.ygyno.2006.10.024

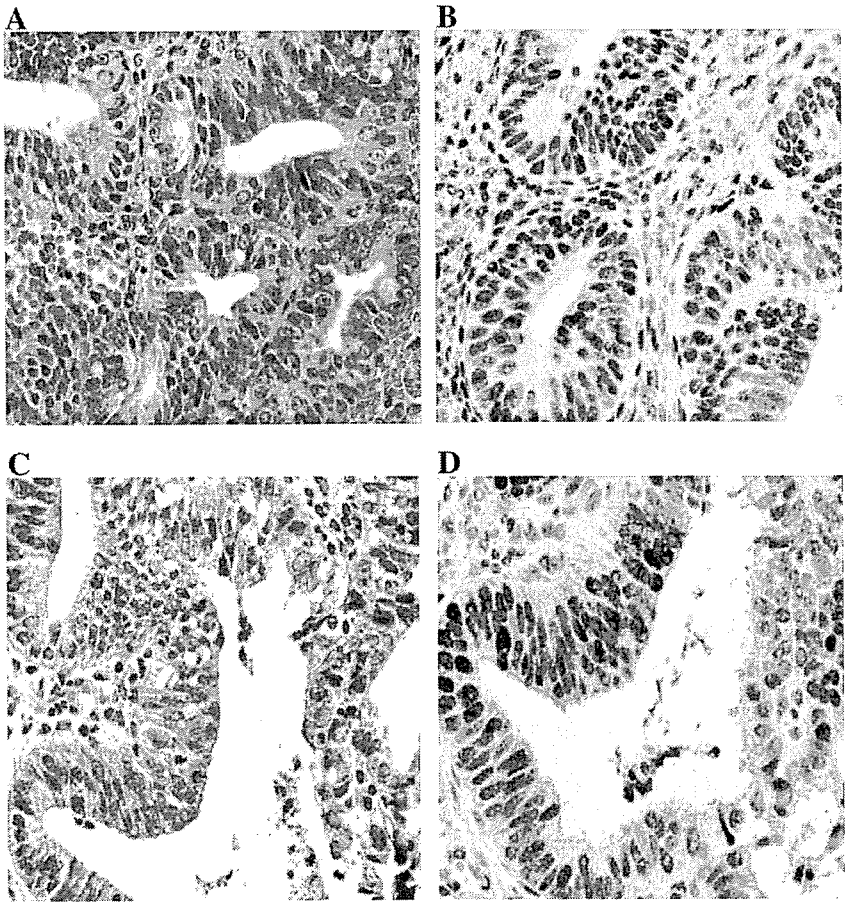

Fig. 1. Histopathology examination of curettaged tissue of endometrium. First curetttaged tissue: (A) hematoxylin and eosin staining showing well-differentiated endometrial adenocarcinoma (magnification ×400), (B) strong positive immunostaining for estrogen receptor (magnification ×400). Second curetttaged tissue: (A) hematoxylin and eosin staining showing remaining focal well-differentiated endometrial adenocarcinoma (magnification ×400), (B) moderate positive immunostaining for estrogen receptor (magnification ×400).

that an endometrial biopsy showed was predominantly estrogen receptor (ER) positive (Fig. 1B). She had a history of polycystic ovary and had received sequential hormone replacement therapy (HRT). Because she desired to preserve her fertility, medical treatment was desirable. In a recent review of women under age 40 with well-differentiated adenocarcinoma, conservative treatment with periodic use of progestin was used [2], and informed consent was obtained from a patient. Before

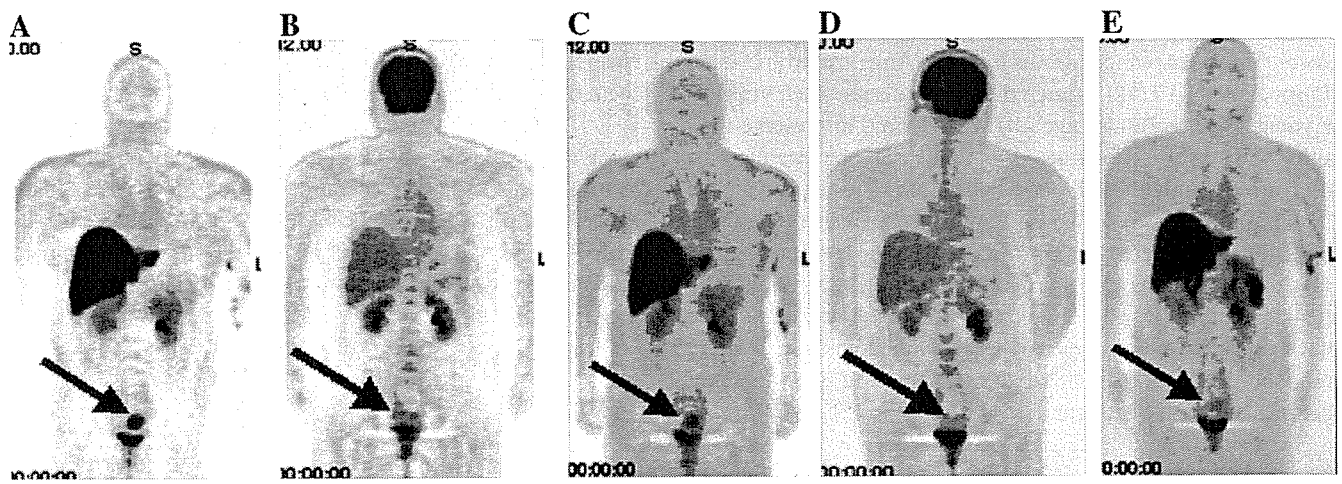

Fig. 2. Endometrial PET during hormonal treatment. Before initiation of treatment: (A) FES-PET showed clearly increased uptake in the endometrium regions and (D) FDG-PET showed slightly increased uptake equivalent to liver uptake. Three months after initiation of treatment, FES-PET showed (B) remaining FES uptake in endometrium site, but (E) FDG-PET showed no abnormal finding. After additional treatment, (C) FES-PET showed no abnormal findings.

progestin treatment was started in our patient, FES-PET showed clearly increased uptake in the endometrium regions; the maximum standardized uptake value (SUV) was 12.5 (Fig. 2A) at late pseudo-secretory phase (day 3 before withdraw bleeding), magnetic resonance imaging (MRI) showed slight thickness of endometrium and FDG-PET showed slightly increased uptake equivalent to liver uptake (Fig. 2B). First, the patient was treated with medroxyprogesterone acetate (MPA) 200 mg per day [6,7]. FES-PET after 3 months showed remaining FES uptake in endometrium site (SUV 6.3) (Fig. 2C), but there were no abnormal findings on MRI and FDG-PET (Fig. 2D). Hysteroscopy and endometrial curettage specimens showed remaining focal well-differentiated adenocarcinoma (Fig. 1C) with moderate ER positivity (Fig. 1D). Next, she was treated with MPA 600 mg per day [6,7]. After more than 3 months, FES-PET showed a therapeutic response (Fig. 2E), and there were no abnormal findings on hysteroscopy and endometrial curettage specimens.

Discussion

To our knowledge, this is the first report showing that FES-PET has the potential to provide functional information about the hormone responsiveness of well-differentiated endometrial adenocarcinoma. When we performed serial FES-PET imaging in a woman with well-differentiated adenocarcinoma treated with MPA, a decrease in FES-PET uptake was seen after a therapeutic response. This decrease correlated with the pathological evaluation. Although the pathological evaluation is the "golden" criteria, FES-PET is a new way to evaluate ER activity in endometrial adenocarcinoma.

The standard method of assessing uterine neoplasms is the formal fractional D & C. But to provide sufficient diagnostic information this method requires that patients are anesthetized [3]. At present, FDG-PET is not incorporated in routine clinical practice for diagnosis of gynecologic cancer or assessment of tumor responsiveness to treatment. However, current clinical applications of FDG in gynecologic cancer diagnosis and management have shown many benefits [8]. On the other hand, the limitation of FDG-PET has been shown to provide lower diagnostic accuracy in detecting minimal lesions as well as some pre-forms of cancer and showing no specificity for cancer detection in general. FDG activity can be seen in the gastrointestinal tract, bladder and inflammatory lesions [8,9].

More than 80% of endometrial cancers are usually associated with a history of unopposed estrogen exposure or other hyperestrogenic risk factors such as obesity [1]. And, it has been well documented that the ER level usually is extremely high especially in well-differentiated endometrial adenocarcinoma. An increased response rate to hormonal agents, including progestin, has been associated with positive estrogen or progesterone receptor status. The PR is a product resulting from estrogen binding to the ER. In some studies, the PR appears to be a better predictor of hormone responsiveness than the ER [2]. Yet, the question is whether FES uptake predicts hormone responsiveness more accurately than does the PR. In this case, FES-PET provided functional information about hormone responsiveness in well-differentiated endometrial adenocarcinoma, similar to that of estrogen dependency of breast cancer.

It is important to take into consideration the cyclic changes in estradiol and estrogen receptor when the potential role of FES-PET in premenopausal women is evaluated because estradiol increases and progesterone decreases ER expression. In this case, FES-PET was performed at late pseudo-secretory phase (day 3 before withdraw bleeding) and showed clearly increased uptake in the endometrium regions. During the physiological cycle or during HRT, ER levels are lower in the secretory phase than in other phases of the cycle [10]. Thus, FES-PET has the potential to provide functional information about ER activity in well-differentiated endometrial adenocarcinoma.

In summary, FES-PET showed increased uptake of FES in well-differentiated endometrial adenocarcinoma and provided information for assessing tumor response to hormonal therapy; FES-PET provided more useful information than did FDG-PET. These observations highlight the need for further systemic studies on the utility of FES-PET in gynecologic cancer.

References

[1] Amant F, Neven P, Timmerman D, Van Limbergen E, Vergote I. Endometrial cancer. Lancet 2005;366:491–505.
[2] Curtin JP, Kavanagh JJ, Fox H, Spanos Jr WJ, Corpus. Mesenchymal tumors. In: William JH, Carlos AP, Robert CY, editors. Principles and Practice of Gynecologic Oncology. 3rd ed. Philadelphia: Lippincott Williams & Wilkins; 1999. p. 961–79.
[3] Pecorelli S, Fallo L, Sartori E, Gastaldi A. Preinvasive lesions of the endometrium. Ann N Y Acad Sci 1991;622:449–62.
[4] Gambhir SS. Molecular imaging of cancer with positron emission tomography. Nat Rev, Cancer 2002;2:683–93.
[5] Linden HM, Stekhova SA, Link JM, Gralow JR, Livingston RB, Ellis GK, et al. Quantitative fluoroestradiol positron emission tomography imaging predicts response to endocrine treatment in breast cancer. J Clin Oncol 2006;24:2793–9.
[6] Randall TC, Kurman RJ. Progestin treatment of atypical hyperplasia and well-differentiated carcinoma of the endometrium in women under age 40. Obstet Gynecol 1997;90:434–40.
[7] Podratz KCO, Brien PC, Malkasian GD, Decker Jr DG, Jefferies JA. Effects of progestational agents in treatment of endometrial carcinoma. Obstet Gynecol 1985;66:106–10.
[8] Kumar R, Alavi A. PET imaging in gynecologic malignancies. Radiol Clin North Am 2004;42:1155–67.
[9] Lerman H, Metser U, Grisaru D, Fishman A, Kievshitz G, Even-Sapir E. Normal and abnormal 18F-FDG endometrial and ovarian uptake in pre- and postmenopausal patients: assessment by PET/CT. J Nucl Med 2004;45:266–71.
[10] Habiba MA, Bell SC, Al-Azzawi F. The effect of hormone replacement therapy on the immunoreactive concentrations in the endometrium of oestrogen and progesterone receptor, heat shock protein 27, and human beta-lactoglobulin. Hum Reprod 2000;15:36–42.

資料(8)

資料 8

Available online at www.sciencedirect.com
SCIENCE DIRECT®

ELSEVIER

Nuclear Instruments and Methods in Physics Research A 563 (2006) 49–53

NUCLEAR INSTRUMENTS & METHODS IN PHYSICS RESEARCH Section A

www.elsevier.com/locate/nima

Studies of the performance of different front-end systems for flat-panel multi-anode PMTs with CsI(Tl) scintillator arrays

H. Sekiya[a,*], K. Hattori[a], H. Kubo[a], K. Miuchi[a], T. Nagayoshi[b], H. Nishimura[a], Y. Okada[a], R. Orito[c], A. Takada[a], A. Takeda[d], T. Tanimori[a], K. Ueno[a]

[a]*Department of Physics, Graduate School of Science, Kyoto University, Kitashirakawa, Sakyo, Kyoto 606-8502, Japan*
[b]*Advanced Research Institute for Science and Engineering, Waseda University, 17 Kikui-cho, Shinjuku, Tokyo 162-0044, Japan*
[c]*Department of Physics, Graduate School of Science and Technology, Kobe University, 1-1 Rokkoudai, Nada, Kobe 657-8501, Japan*
[d]*Kamioka Observatory, ICRR, University of Tokyo, 456 Higasi-mozumi, Hida-shi, Gifu 506-1205, Japan*

Available online 20 February 2006

Abstract

We have studied the performance of two different types of front-end systems for our gamma camera based on Hamamatsu H8500 (flat-panel 64 channels multi-anode PSPMT) with a CsI(Tl) scintillator array. The array consists of 64 pixels of $6 \times 6 \times 20\ mm^3$ which corresponds to the anode pixels of H8500.

One of the system is based on commercial ASIC chips in order to read out every anode. The others are based on resistive charge divider network between anodes to reduce readout channels. In both systems, each pixel (6 mm) was clearly resolved by flood field irradiation of ^{137}Cs. We also investigated the energy resolution of these systems and showed the performance of the cascade connection of resistive network between some PMTs for large area detectors.

PACS: 85.60.H; 87.62; 87.59; 95.55.K

Keywords: Flat-panel detector; PSPMT; Gamma camera; Compton telescope

1. Introduction

Recently, the concern with the gamma camera based on position-sensitive PMTs for application especially to nuclear medicine has been growing. The latest developed flat-panel-type Hamamatsu H8500 and H9500 [1] are promising devices for such purpose, and several studies have been conducted focusing on their spatial resolution with both pixellated scintillator array and continuous scintillator slab aiming at PET and SPECT applications [2–4].

The merit of such multi-anode flat-panel-type PMTs is the small non-active area when they are arrayed and constitute large area detectors, however, developments of readout systems for large number of channels are indispensable.

On the other hand, Compton imaging detectors for gamma ray astronomy or next generation medical imaging has been developed [5–7] with gamma cameras used for the detection of scattered gamma rays. In such cases, not only the spatial resolution but also the energy resolution is important to reconstruct the direction of incident gamma rays.

In this paper, we report the spatial resolution and energy resolution of our gamma camera based on H8500 with two different types of front-end systems. One of the system is based on commercial ASIC chips in order to read out every anode, the others are based on the resistive charge divider network between anodes to reduce the readout channels. In order to evaluate the performance, we coupled a CsI(Tl) scintillator array which fits to the anode pitches of H8500. This camera is intended for arrayed and covering our

*Corresponding author. Tel.: +81 75 753 3868; fax: +81 75 753 3799.
E-mail address: sekiya@cr.scphys.kyoto-u.ac.jp (H. Sekiya).

0168-9002/$ - see front matter © 2006 Elsevier B.V. All rights reserved.
doi:10.1016/j.nima.2006.01.096

micro-time projection chamber (micro-TPC) [5], which constitutes a new Compton imaging detector [8].

2. The detector

The Hamamatsu H8500 has a very compact dimension of 52 mm × 52 mm × 28 mm with 12 stages of metal channel dynodes and a HV divider circuit. The active photo cathode area is 49 mm × 49 mm and is covered by an 8 × 8 anode array. The typical anode gain is 10^6 (HV = −1000 V) and the typical anode gain uniformity (the ratio of the maximum gain to the minimum gain) is about 2.5. Each anode pixel size is 5.8 mm × 5.8 mm and the pitch between center of the anodes is 6.08 mm.

The size of each CsI(Tl) crystal is 6 mm × 6 mm × 20 mm. The crystals were also manufactured by Hamamatsu. Between the crystals, Vikuiti® ESR films (3M) of 65 μm are inserted for the optical isolation, so that the pixel of scintillator array corresponds to the anode pixel. The array is glued to H8500 using OKEN6262A optical grease. Fig. 1 shows the picture of the array.

3. Readout circuits

3.1. CP80068 system

Fig. 2 shows the individual anode readout system (Clear Pulse Co., Ltd. CP80068). The dimension of CP80068 which is designed for two-dimensional array of H8500 is 52 mm × 52 mm × 95 mm. It is based on two types of analog ASICs, VA32HDR14 and TA32CG2 manufactured by IDEAS ASA. VA32HDR14 contains pre-amplifiers (input dynamic range ~ ± 15 pC), shapers (gain = 118 mV/pC, peaking time = 2 μs), sample and hold circuits and a multiplexer. TA32CG32 contains fast shapers (peaking time = 75 ns) and comparators, which can make the trigger signals. The multiplexed 64 ch data are digitized by a flash ADC on the CP80068 and sent to the VME sequence module via FPGAs. It takes 164 μs to process one event (64 channels).

3.2. Resistive charge division

Fig. 3 shows the charge divider network board for H8500. Using this connector board, the anodes in

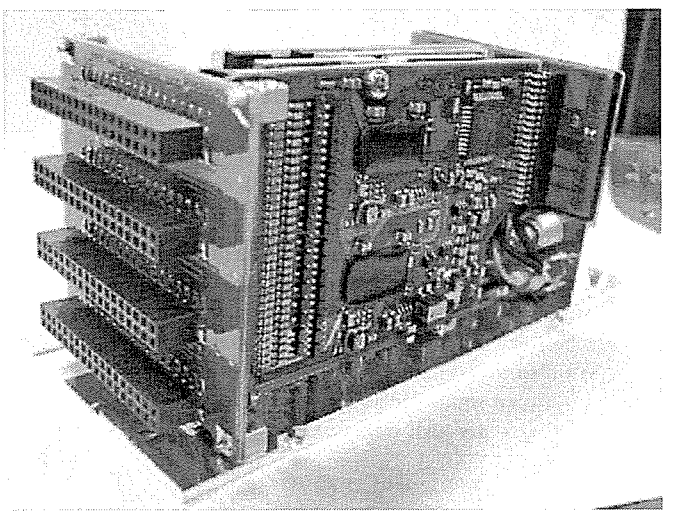

Fig. 2. Picture of CP80068.

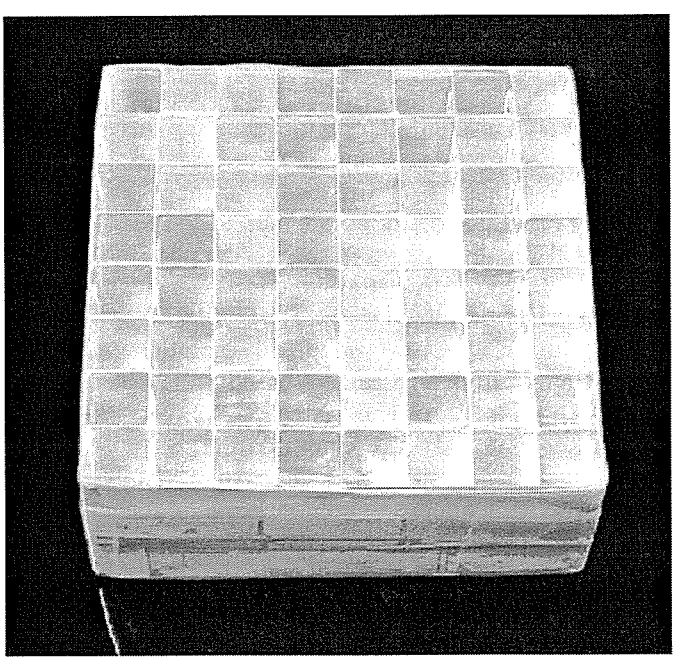

Fig. 1. Picture of the CsI(Tl) array.

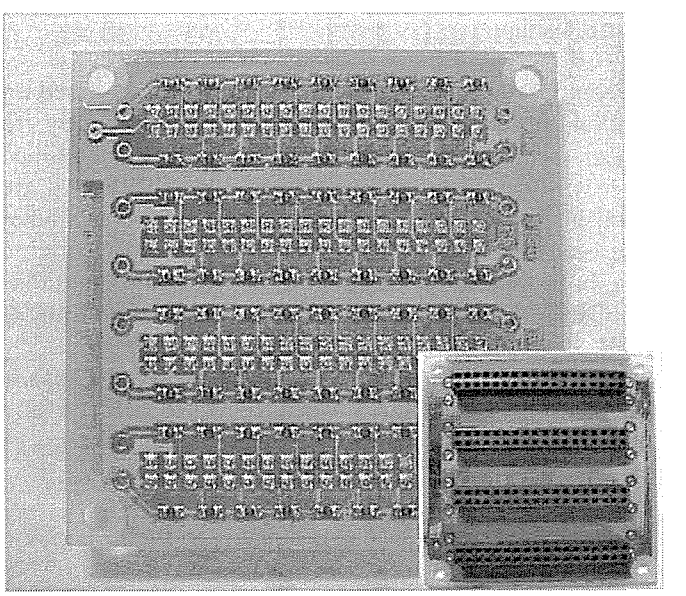

Fig. 3. Bottom view of the resistive divider network for H8500 and the top view (inset).

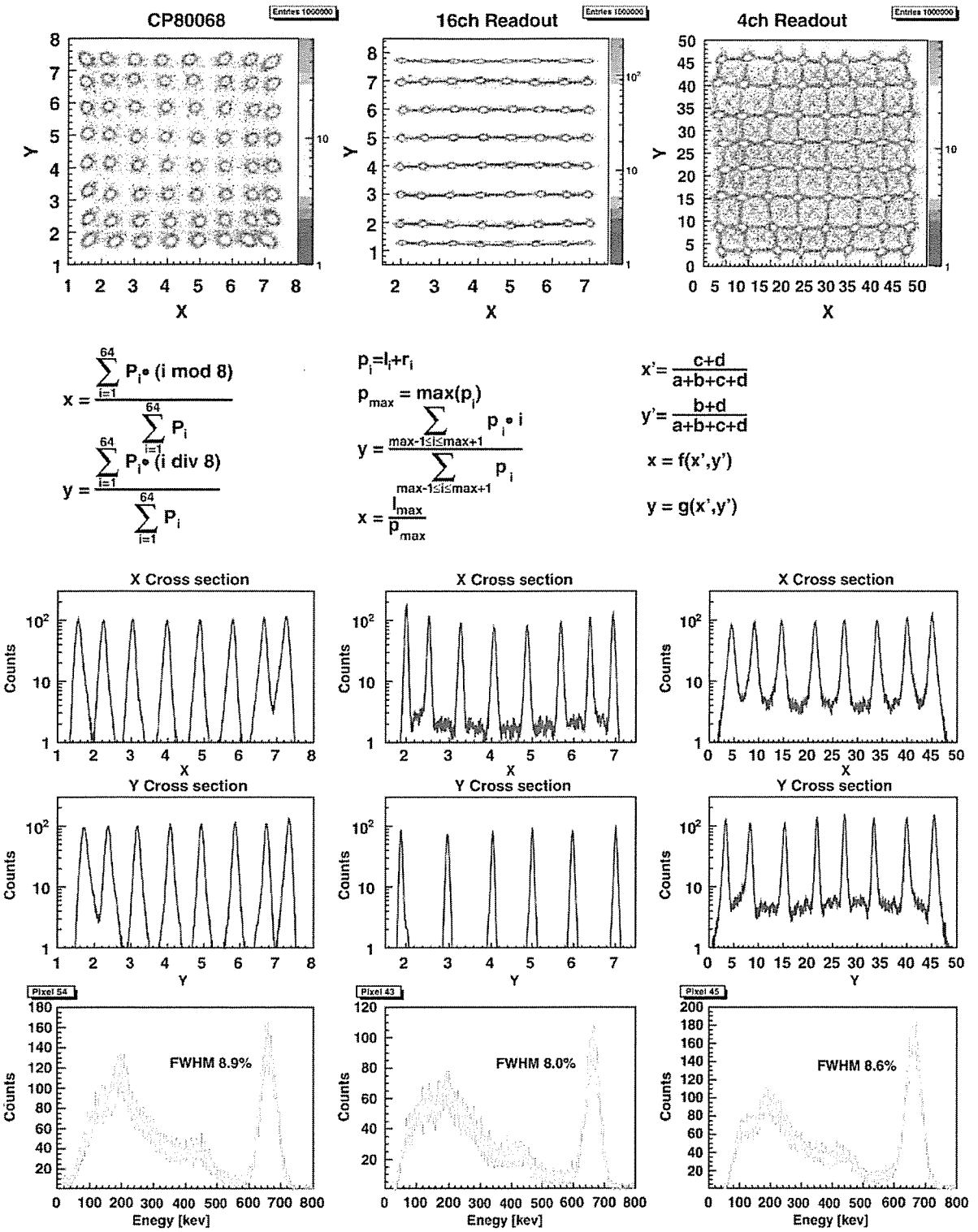

Fig. 4. Measurement results of each readout system. Flood field images of ^{137}Cs irradiation, methods of the position reconstruction, x and y cross-sections of central rows, the energy spectra of the best pixel of every readout system are shown. In the equations, P_i is the ADC output of ith anode of CP80068 system, $l_i(r_i)$ is the ADC output of left (right) side of ith horizontal resistive chain of 16 channels readout system, $a \cdot b \cdot c \cdot d$ represent the ADC outputs of four terminals of four channels readout system. In four channels readout system, as the raw image (x', y') is distorted, the corrected image (x, y) calculated by TMultiDimFit class of ROOT [9] is indicated.

horizontal rows of H8500 are connected with 100 Ω chips and the number of readout channels are reduced to 16. Each reduced channel is preamplified (integrating time constant = 66 μs), shaped (Clear Pulse CP4026, shaping time = 2 μs) and digitized (CAEN V785). The last dynode output is used as the trigger signal.

Table 1
Measured 662 keV energy resolutions (FWHM) of the pixels in each readout system

System	Best (%)	Typical (%)	Worst (%)
CP80068	8.9	9.5	10.0
16 ch readout	8.0	8.7	9.5
Four ch readout	8.6	8.8	9.9

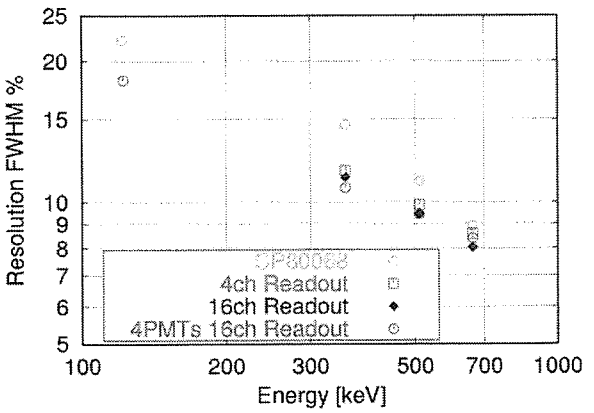

Fig. 5. Measured energy resolution of the best pixels of all the readout systems. Results of "4PMTs 16 ch Readout" explained in Fig. 6 are also indicated.

For further reduction of the readout channels, we connected the intervals of the both edges of the horizontal chains with 100 Ω resistors, thus four channels readout with resistive chain is also tested.

4. Measurements and results

We are interested in the energy of sub-MeV region [5], accordingly, the CsI(Tl) array was irradiated by 1 MBq ^{137}Cs source (662 keV) at a distance of 30 cm. For the energy calibration, ^{22}Na (511 keV), ^{133}Ba (356 keV) and ^{57}Co (122 keV) were also used. An important point to mention here is the dynamic ranges of the readout circuits. As the input dynamic range of CP80068 is as small as −15 pC, H8500 should be operated with the gain of 10^4 (HV~600 V) to observe 662 keV gamma rays. In the case of resistive charge division circuits, dynamic ranges of the shaper and the ADC also limit the operation gain of H8500 to 10^5 (HV~800 V).

4.1. Spatial resolution

The obtained flood irradiation images of ^{137}Cs are shown in Fig. 4. The methods of the calculation of the position reconstruction are indicated as well. Image spots represent pixels of the CsI(Tl) array, which indicates that the intrinsic spatial resolution of H8500 is better than the anode pixel size.

The accidental hit events of multi-pixels were rejected in the results of CP80068 system (selection efficiency was

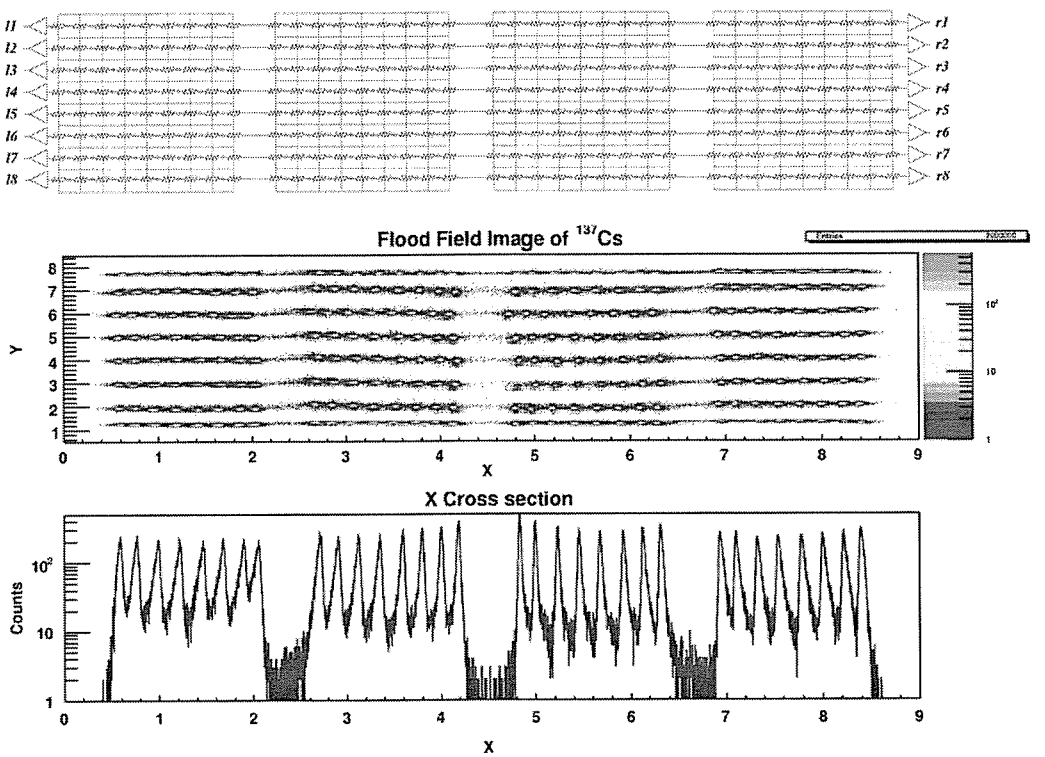

Fig. 6. Cascade connection of four H8500s with resistive charge divider network.

79%) and the accidental hit events of more than two horizontal rows were also rejected in the results of the 16 channels readout system (selection efficiency was 85%). On the other hand, in the four channels readout system, there is no way to reject such events; therefore, the peak to valley ratios of the x/y cross-section of the flood irradiation image are the worst.

4.2. Energy resolution

The obtained energy spectra of the best pixel of each readout system are also shown in Fig. 4. The variations of the energy resolution of 662 keV of every readout system are summarized in Table 1.

The variation of the resolution is mainly due to the variation of the anode gain. Near the boundary of the detection area, optical leakage (photon collection inefficiency) also affects not only the energy resolution but also the spatial resolution. Fig. 5 shows the energy resolutions of measured energy of all the readout systems. The reason why the energy resolution of the result of CP80068 system is the worst is its low HV operation.

5. Discussion and conclusion

It is admitted that individual anode readout is the best way for multi-anode PMTs, however, that needs development of exclusive ASICs with consideration for the light outputs of scintillator, gain of the PMT, and the dynamic range. Moreover, in our case, the spatial resolution is not determined by the anode pixel size but by the crystal pixel size.

Therefore, the advantage of energy resolution of the resistive charge divider network and discrete modules of readout circuit is encouraging to make larger area detector. We made cascade resistive connection of four H8500s as shown in Fig. 6, for example. The energy resolution is also shown in Fig. 5. This connection is another example of four channels/PMT readout and crystal pixel identification is better than that of previous four channels readout system.

In conclusion, large area detector of pixel scintillator and H8500 array with resistive charge division systems have a good performance both energy and spatial resolutions and have many possibilities in medical and gamma ray astronomy applications.

Acknowledgement

We would like to thank Takahashi Lab. at Institute of Space and Astronautical Science, Japan Aerospace Exploration Agency, Makishima Lab. at Department of Physics, School of Science, University of Tokyo and Dr. Gunji for the development of CP80068.

References

[1] Hamamatsu technical data sheet H8500-H8500B, H9500, February 2005, printed in Japan, ⟨http://www.hamamatsu.com⟩.
[2] R. Pani, et al., Nucl. Instr. and Meth. A 527 (2004) 54;
R. Pani, et al., Nucl. Instr. and Meth. A 513 (2003) 36.
[3] M. Giménez, et al., Nucl. Instr. and Meth A 525 (2004) 298.
[4] D. Herbert, et al., Nucl. Instr. and Meth. A 518 (2004) 399.
[5] A. Takada, et al., Nucl. Instr. and Meth. A 546 (2005) 258.
[6] G. Kanbach, et al., Nucl. Instr. and Meth. A 541 (2005) 310.
[7] A. Studen, et al., Nucl. Instr. and Meth. A 531 (2004) 258.
[8] T. Tanimori, et al., New Astron. Rev. 48 (2004) 263.
[9] ROOT, An object-oriented analysis framework, ⟨http://root.cern.ch⟩.

資料(9)

Available online at www.sciencedirect.com
ScienceDirect
ELSEVIER
Nuclear Instruments and Methods in Physics Research A 573 (2007) 115–118
NUCLEAR INSTRUMENTS & METHODS IN PHYSICS RESEARCH Section A
www.elsevier.com/locate/nima

Development of large area gamma-ray camera with GSO(Ce) scintillator arrays and PSPMTs

H. Nishimura[a,*], K. Hattori[a], S. Kabuki[a], H. Kubo[a], K. Miuchi[a], T. Nagayoshi[b], Y. Okada[a], R. Orito[c], H. Sekiya[a], A. Takada[a], A. Takeda[d], T. Tanimori[a], K. Ueno[a]

[a]*Department of Physics, Graduate School of Science, Kyoto University, Kitashirakawa-oiwake, Sakyo, Kyoto 606-8502, Japan*
[b]*Advanced Research Institute for Science and Engineering, Waseda University, 17 Kikui-cho, Shinjyuku, Tokyo 162-0044, Japan*
[c]*Department of Physics, Graduate School of Science and Technology, Kobe University, 1-1 Rokkoudai, Nada, Kobe 657-8501, Japan*
[d]*Kamioka Observatory, ICRR, University of Tokyo, 456 Higasi-mozumi, Hida-shi, Gifu 506-1205, Japan*

Available online 29 November 2006

Abstract

We have developed a position-sensitive scintillation camera with a large area as an absorber of an advanced Compton gamma-ray camera. At first we tested GSO(Ce) crystals. We compared light output from the GSO(Ce) crystals under various conditions: the method of surface polishing, the concentration of Ce, and co-doping Zr. As a result, we chose the GSO(Ce) crystals doped only 0.5 mol% Ce, surface of which was polished by chemical etching for the scintillator of our camera. We also made a $16 \times 16\,cm^2$ scintillation camera which consisted of nine position-sensitive PMTs (PSPMTs Hamamatsu flat-panel H8500), the each of which had 8×8 anodes with a pitch of 6 mm and coupled to 8×8 arrays of pixelated $6 \times 6 \times 13\,mm^3$ GSO(Ce) scintillators. For the readout system of 576 anodes of the PMTs, we used chained resistors to reduce the number of readout channels down to 48 for saving power consumption. The camera has the position resolution of less than 6 mm and a typical energy resolution of 10.5% (FWHM) at 662 keV at each pixel in a large area of $16 \times 16\,cm^2$.

Furthermore, we constructed a 16×16 array of $3 \times 3 \times 13\,mm^3$ pixelated GSO(Ce) scintillators, and glued it to a PMT H8500. This camera had the position resolution of less than 3 mm in area of $5 \times 5\,cm^2$, except for some of edge pixels; the energy resolution was typically 13% (FWHM) at 662 keV.

PACS: 85.60.Ha; 87.58.Pm; 95.55.Ka

Keywords: GSO(Ce); Gamma-ray camera; PSPMTs

1. Introduction

We have been developing an advanced Compton camera for gamma-ray astronomy in the range of 100 keV to 20 MeV [1]. It needs a scintillation camera as a detector for Compton-scattered gamma rays, which has good energy and position resolution and a large area because the resolution and the efficiency for the scattered gamma rays contribute to the angular resolution and the efficiency of the advanced Compton camera. In addition, radiation hardness and a high counting-rate performance of the scintillation camera are required. For these requirements, we chose a GSO(Ce) (Gd_2SiO_5 : Ce) crystal as a scintillator, and the PSPMT H8500 (Flat Panel PMT produced by Hamamatsu [2]) as a position-sensitive photon device.

GSO(Ce) has advantages in astronomical use, such as having a higher-Z, faster decay time than NaI(Tl), a higher light output than BGO, greater radiation hardness and less radioactivation than most of the known scintillators. Furthermore, GSO(Ce) can be easily cut and polished, since it is nonhydroscopic.

The PSPMT H8500 was recently developed as a promising device for nuclear physics and medicine, for example, PET and SPECT [3–6]. It has 8×8 anodes with a 6 mm pitch and 12-stage metal channel dynodes. The

*Corresponding author. Tel.: +81 75 753 3869; fax: +81 75 753 3799.
E-mail address: nisimura@cr.scphys.kyoto-u.ac.jp (H. Nishimura).

0168-9002/$ - see front matter © 2006 Elsevier B.V. All rights reserved.
doi:10.1016/j.nima.2006.11.029

advantage of this PMT is that it has a much smaller dead space and a larger effective area than that of the previous multi-anode PMTs. The effective area of this PMT is $49 \times 49\,mm^2$, which is 89% of the package size.

In this paper we report on the result of measurements of pixelated GSO(Ce) scintillators and the performances (energy resolution and position resolution) of our developed scintillation camera.

2. Measurements of pixelated GSO(Ce) scintillators

There are some conditions that characterize the performance of a pixelated GSO(Ce) scintillator. One is the pixel size. The width of 6 mm and the thickness of 13 mm were chosen for our scintillation camera in order to fit the pitch of the anodes of PSPMTs, and the radiation length. One of the other important issues is the method of surface polishing. There are two established methods of polishing: one is chemical etching, and the other is mechanical polishing. It was reported that there was little difference between the performances of pixelated scintillators polished with these methods [7]. However, mechanical polishing is more expensive than chemical etching. Another important issue is the concentration of Ce as a scintillation activity impurity, and additional dopants. The light-decay time becomes faster as the concentration of Ce increases, although increasing the concentration of Ce decreases the optical transmittance of the crystal. It was also reported that doping 200 ppm of Zr to GSO(Ce) improved the optical transmittance of the crystal [8].

We measured the light outputs from several crystals under different conditions of polishing or doping impurity in order to examine how effective these conditions were. There were eight types of pixelated scintillators, which were different at the point of the concentration of Ce, the existence of Zr, and the ingot. We enveloped each pixel scintillator by a reflector (Goatex) and coupled the crystal face with an area of $6 \times 6\,mm^2$ or $4 \times 6\,mm^2$ to a single anode PMT (R6231 Hamamatsu) with the optical grease (OKEN 6262). We then irradiated it with 662 keV gamma rays from a ^{137}Cs source through a $\varnothing 3$ mm collimator. Fig. 1 shows the relative light outputs and energy resolution at 662 keV. The systematic errors were due to the reproducible errors of the condition of crystal with the reflector or the condition of gluing. It shows that the method of polishing and the optical transmittance caused by the concentration of Ce are not more effective for the performance of our pixel size of $6 \times 6 \times 13\,mm^3$ than the difference of the ingot. However, there is a significant difference between only 1 mol% Ce doped crystals with a size of $4 \times 6 \times 20\,mm^3$ and the others. This shows a significant decreasing of the optical transmittance caused by Ce and the improvement of transmittance caused by doping Zr for longer crystal with a thickness of 20 mm.

From the above studies, we chose crystals that were polished by chemical etching and doped only Ce-0.5 mol% for our camera. We made an 8×8 array of pixelated GSO(Ce) scintillators. Each pixel was optically separated by Vikuiti 3M ESR, which is a multilayer polymer mirror with a thickness of 65 μm and a reflectance of 98%. The construction of this array is described in Ref. [6].

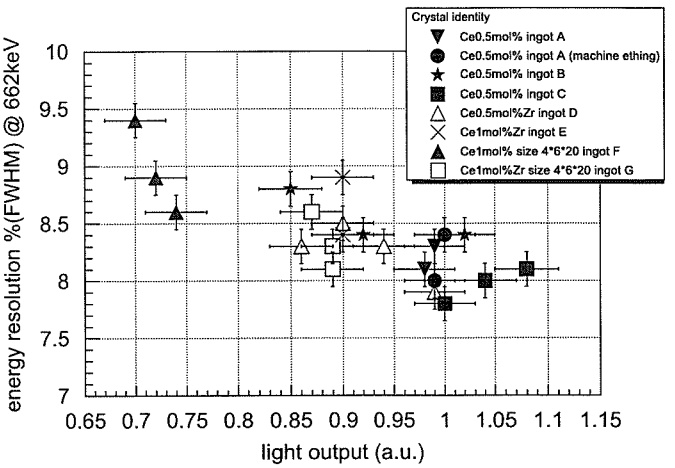

Fig. 1. Light output and energy resolution of pixelated GSO(Ce) scintillators with or without a Zr dopant. The systematic errors are also shown.

3. Performance of a $5 \times 5\,cm^2$ scintillation camera and a $16 \times 16\,cm^2$ scintillation camera

We made a $5 \times 5\,cm^2$ scintillation camera by coupling an 8×8 GSO(Ce) array to a PMT H8500 with grease. In order to save power consumption, the readout circuit of the camera consisted of eight resistive chains, 16 ch amplifiers, and ADCs, as described in Ref. [9].

The image of each pixel scintillator was clearly resolved by a flood field of irradiation of 662 keV gamma ray, which means that the position resolution was less than a pixel pitch of 6 mm. Furthermore, we also obtained the energy spectrum of each pixel with energy resolution of 10% (FWHM) @ 662 keV.

This $5 \times 5\,cm^2$ camera can be easily extended to a larger camera. We constructed a $16 \times 16\,cm^2$ camera with 3×3 PMTs, as shown in Fig. 2. The pitch of PMTs was 53 mm and the effective area of the camera is 82%. The number of readout channels of the camera was only 48 channels with 24 resistive chains. All 576 pixels were clearly resolved by a flood field of radiation of 662 keV gamma ray, as shown in Fig. 3(a) and (b), which are an event map and an x-projection map at the 12th row ($78\,mm < y < 84\,mm$), respectively. The events located between each pixels seem to be multi-pixel hits events by Compton-scattered gamma ray or accidental events. The energy resolution (FWHM) was 31.0% at 122 keV, 18.2% @356 keV, 13.9% @511 keV, 10.7% @662 keV, 9.6% @835 keV, 8.6% @1173 keV for the typical pixel, 9.8%@662 keV(FWHM) for good pixels and 13%@662 keV(FWHM) for bad pixels. Fig. 4 shows a map of the relative light output at each pixel. It mainly shows differences among anode

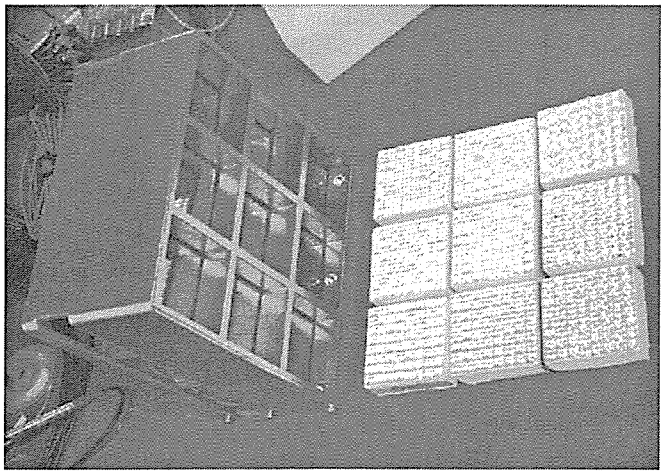

Fig. 2. Photograph of a $16 \times 16\,cm^2$ scintillation camera composed of nine PSPMTs, the each of which coupled to 8×8 arrays of pixelated $6 \times 6 \times 13\,mm^3$ GSO(Ce) crystals.

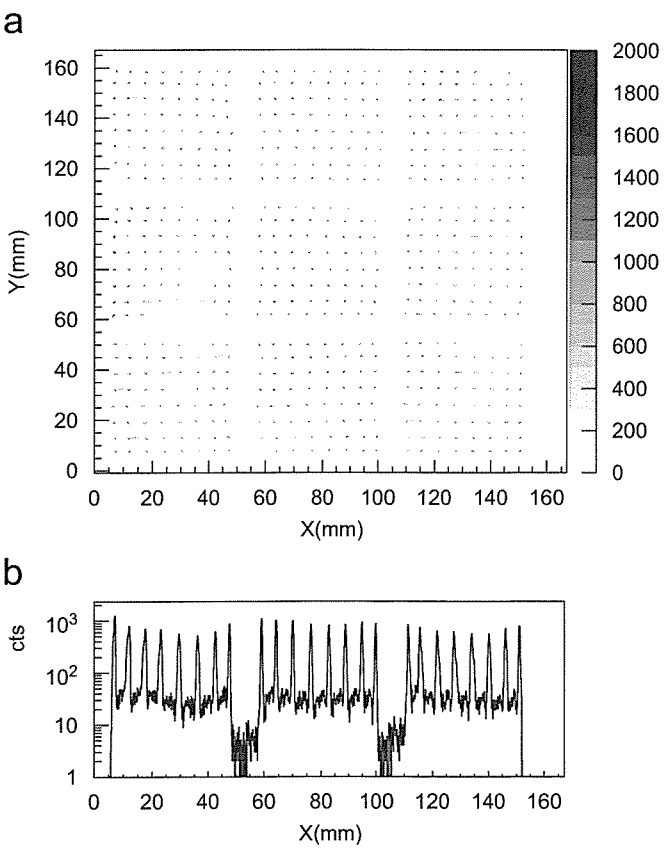

Fig. 3. (a) Event map measured with the $16 \times 16\,cm^2$ scintillation camera in a flood of irradiation of 662 keV gamma rays. (b) The logarithmic x-projection of the event map at the 12th row ($78\,mm < y < 84\,mm$).

gains of the PMTs. However, the light output was too low at some edges of each PMT. This was probably due to a misalignment of the array of crystals to the PMTs. The measurable energy ranges of this camera are 80–1300 keV and 100–900 keV, at good and bad pixels, respectively.

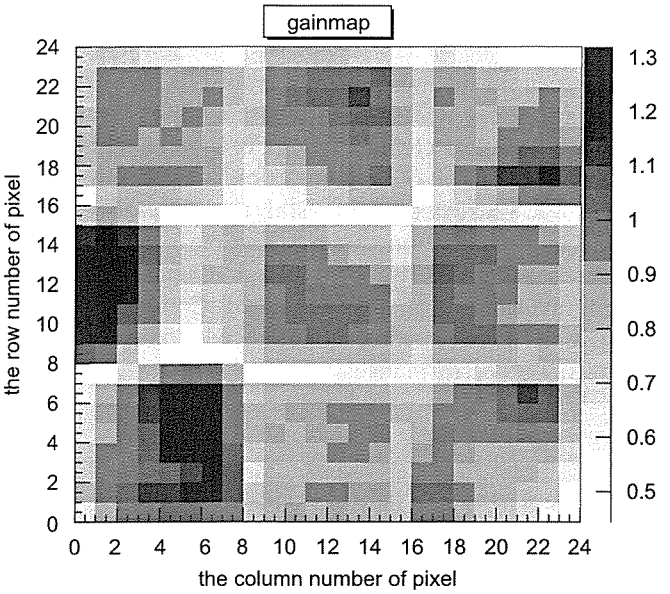

Fig. 4. Distribution of the light outputs for the $16 \times 16\,cm^2$ scintillation camera composed of arrays of $6 \times 6 \times 13\,mm^3$ GSO(Ce) pixelated crystals.

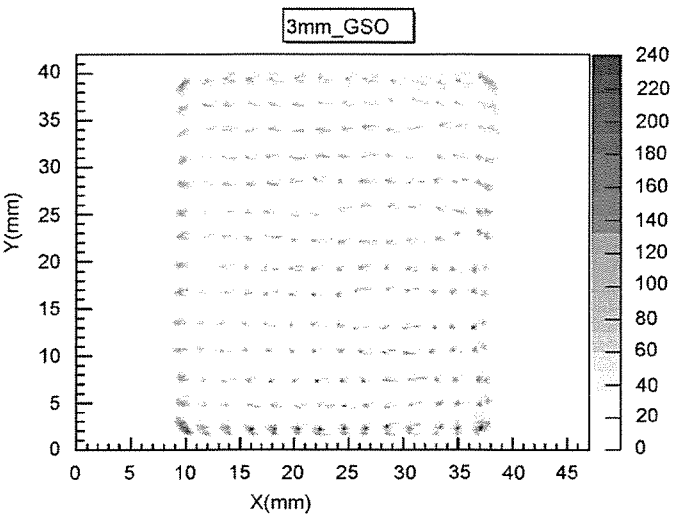

Fig. 5. Event map measured with a scintillation camera composed of a 16×16 array of $3 \times 3 \times 13\,mm^3$ pixelated GSO(Ce) crystals and a H8500.

In order to improve the position resolution, we tried to use smaller pixels with a width of 3 mm compared to that of the anode pitch of H8500. Such developments were already reported by papers [3–5]. We made a 16×16 array of pixelated $3 \times 3 \times 13\,mm^3$ GSO(Ce) scintillators and coupled it to the H8500. In the flood field of irradiation of 662 keV gamma rays, the pixel image was clearly separated, except for some of edge pixels, as shown in Fig. 5. However, the energy resolution became worse to 12% @662 keV than one of scintillation cameras with $6 \times 6 \times 13\,mm^3$ pixels.

4. Summary

We measured the light outputs from GSO(Ce) scintillators under some different conditions, and chose a Zr nondoped chemical etching GSO(Ce) crystal with size of $6 \times 6 \times 13\,mm^3$ for our scintillation camera. We constructed 8×8 arrays of the crystal, and developed a $16 \times 16\,cm^2$ GSO scintillation camera. The performance of this camera is sufficient to use as an Compton-scattered gamma-ray camera of our advanced Compton camera. We have been constructing an advanced Compton camera and testing its performance.

Acknowledgments

This work is supported by a Grant-in-Aid for the 21st Century COE "Center for Diversity and Universality in Physics"; a Grant-in-Aid in Scientific Research of the Japan Ministry of Education, Culture, Science, Sports, Technology; "SENTAN", JST. We thank Dr. Y. Yanagida and Hitachi Chemical, Co. Ltd. for their support.

References

[1] A. Takada, et al., Nucl. Instr. and Meth. A 546 (2005) 258.
[2] Hamamatsu technical data sheet H8500-H8500B, February 2005, printed in Japan, ⟨http://www.hamamatsu.com⟩.
[3] R. Pani, et al., Nucl. Instr. and Meth. A 527 (2004) 54; Nucl. Instr. and Meth. A 513 (2003) 36.
[4] M. Gimenez, et al., Nucl. Instr. and Meth. A 525 (2004) 298.
[5] D. Herbert, et al., Nucl. Instr. and Meth. A 518 (2004) 399.
[6] N. Inadama, et al., IEEE Trans. Nucl. Sci. NS-51 (1) (2004) 58; IEEE Trans. Nucl. Sci. NS-52(1) (2005) 15.
[7] K. Kurashige, et al., IEEE Trans. Nucl. Sci. NS-45 (3) (1998) 522.
[8] Hitachi, chemical Technical Report No.44 13 (2005-1), Printed in Japan, ⟨http://www.hitachi-chem.co.jp/japanese/report/⟩.
[9] H. Sekiya, et al., Nucl. Instr. and Meth. A 563 (2006) 49.

資料（10）

Available online at www.sciencedirect.com
ScienceDirect
ELSEVIER
Nuclear Instruments and Methods in Physics Research A 573 (2007) 195–199
NUCLEAR INSTRUMENTS & METHODS IN PHYSICS RESEARCH Section A
www.elsevier.com/locate/nima

A very large area Micro Pixel Chamber

A. Takada[a,*], K. Hattori[a], S. Kabuki[a], H. Kubo[a], K. Miuchi[a], T. Nagayoshi[b], H. Nishimura[a], Y. Okada[a], R. Orito[c], H. Sekiya[a], A. Takeda[d], T. Tanimori[a], K. Ueno[a]

[a]*Cosmic-Ray group, Department of Physics, Graduate School of Science, Kyoto University, Japan*
[b]*Waseda University, Japan*
[c]*Kobe University, Japan*
[d]*ICRR, University of Tokyo, Japan*

Available online 27 November 2006

Abstract

A Micro Pixel Chamber, called "μ-PIC", is a gaseous 2D imaging detector with a fine pixel electrode based on the Printed Circuit Board technology, and we developed it for the X/gamma-ray imaging and the tracking of the charged particles [A. Ochi, et al., Nucl. Instr. and Meth. A 478 (2002) 196; T. Nagayoshi, et al., Nucl. Instr. and Meth. A 525 (2004) 20.]. The previous μ-PIC has a fine position resolution, a high gas gain, a good gas gain uniformity and the stable operation. Although the detection area of the previous μ-PIC ($\sim 10 \times 10\,cm^2$) is not large enough for a variety of the application, for example an MeV gamma-ray Compton camera [T. Tanimori, et al., New Astron. Rev. 48 (2004) 263.] and dark matter search [T. Tanimori, et al., Phys. Lett. B 578 (2004) 241.]. Therefore, we developed a new μ-PIC having a $\sim 30 \times 30\,cm^2$ detection area. The structure and the pitch of the electrode are same as those of the previous μ-PIC. There are 768 × 768 pixels in the whole area. This μ-PIC (TOSHIBA SN041129-1) is operated with a stable gas gain of ~3500 and a maximum gain of ~7000 at the center region, and the variety of the gain was 16.7% RMS. An X-ray image of the whole area was also taken by the irradiation of the X-rays from ^{109}Cd (22 keV) to the whole detection area.

PACS: 29.40.Cs; 29.40.Gx; 87.59.−e

Keywords: Gaseous detector; μ-PIC; Micro-pattern detector; X-ray imaging

1. Introduction

A Micro Pixel Chamber (μ-PIC) is a gaseous 2D imaging detector with a fine pixel electrode based on the Printed Circuit Board technology, and we developed it for the X-ray imaging and the tracking of the charged particles [1]. The pixel electrode of the μ-PIC is placed with a pitch of 400 μm, as shown in Fig. 1, and each pixel works as a proportional counter. Until now, we developed a μ-PIC having a detection area of $10.24 \times 10.24\,cm^2$ and 256 × 256 pixels. The previous μ-PIC has a fine position resolution (RMS ~120 μm), a high gas gain (Max ~15000), a good gas gain uniformity (4.5% RMS) and the stable operation more than 1000 hour with a gas gain of ~6000.

Making good use of the characters of the μ-PIC, we are applying to a μ-PIC to the several developments for an MeV Compton camera [2], the experiment of the dark matter search [3] and the X-ray crystallography [4], but the detection area is not large enough for those applications. Therefore, we have developed a new μ-PIC having a larger detection area.

2. The first production

We obtained the first production of a μ-PIC with a detection area of $30.72 \times 30.72\,cm^2$ in November 2004 (TOSHIBA SN041129-1, Fig. 2). The structure of the pixel electrode is same as that of the previous μ-PIC. There are 768 × 768 pixels (= 589824 pixels) in the whole area, and the pitch of the pixels is 400 μm, that is also same as the previous one. Therefore, the new μ-PIC has a 9 times detection area and a fine position resolution as well as the

*Corresponding author. Tel: +81 75 753 3869; fax: +81 75 753 3799.
E-mail address: takada@cr.scphys.kyoto-u.ac.jp (A. Takada).

0168-9002/$ - see front matter © 2006 Elsevier B.V. All rights reserved.
doi:10.1016/j.nima.2006.10.283

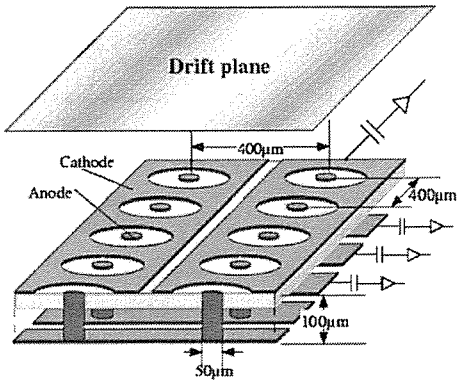

Fig. 1. The structure of μ-PIC.

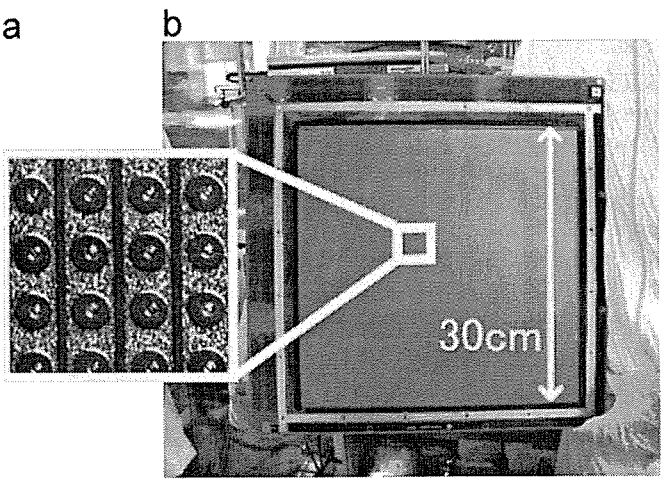

Fig. 2. The photo of the new μ-PIC (TOSHIBA SN041129-1): (a) a micrograph of the pixel electrodes, and the whole detector is (b).

previous one. The anode strips and the cathode strips are connected to the read-out board with the wire bonding one by one, so that we can take the signals from all strips.

The pixel electrode of this μ-PIC is manufactured by the following process: the first process is the electroless plating for creating the seeds of via-fill plating. Next is the via-fill plating, in which the anode holes are filled up and the polyimide substrate are coated with copper. Then, copper is etched to obtain a flat surface. Finally, the pixel electrodes are created by the etching. Now, the yield of the μ-PIC of which the functional pixel rate is above 95% is about 50% in the first production.

The created pixels are classified into the three groups.

(i) Good pixels: The structure of the pixel is ideal, and these pixels make the stable operation. The majority of the pixels is classified into this type.
(ii) Dead pixels: The dead pixels are due to the plating miss. The anode hole of the dead pixel is not filled up, as shown in Fig. 3(a), and the electric field does not concentrate to the center of the pixel. Because the anode electrode is not created, there is no electron avalanche and no signals.
(iii) Bad pixels: The bad pixels are due to the etching miss. The bad pixel has a protrusion on the edge of the cathode electrode, as shown in Fig. 4(a). On the surrounding of the protrusion, the electric field is too strong to suppress the discharge.

Fig. 3(c) shows the distribution of the dead pixels. In the most of the detection area, the rate of the dead pixels is less than 0.1%. But the rate is much higher near the edge area, and that of the worst area, which is the left-lower area of $3 \times 5\,\mathrm{cm}^2$ in Fig. 3(c), is ~40%. In the whole area, the average of the dead pixels rate is about 1%, and it is not a serious problem for the imaging of the X-rays. The positions

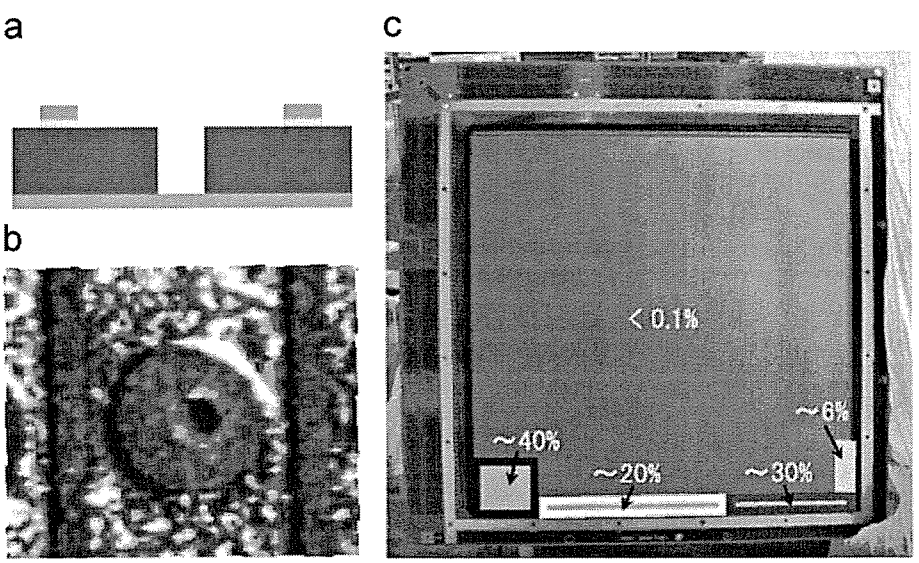

Fig. 3. The photo and the distribution of the dead pixels: (a) a schematic view of the dead pixel, and (b) shows a typical dead pixel. The distribution of the dead pixels is shown in (c).

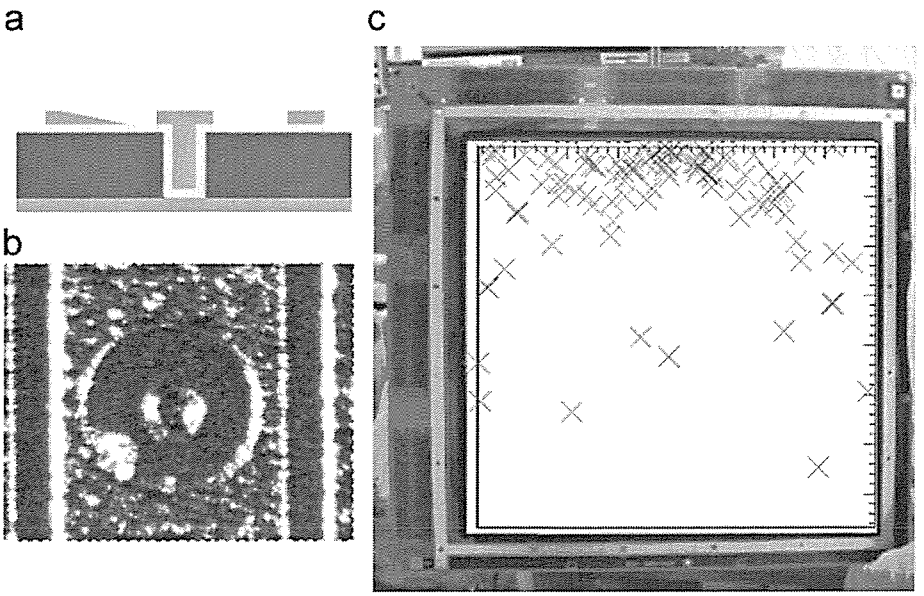

Fig. 4. The photo and the distribution of bad pixels. A schematic view is (a) a typical bad pixel is (b) and the positions of the bad pixels are shown by cross in (c).

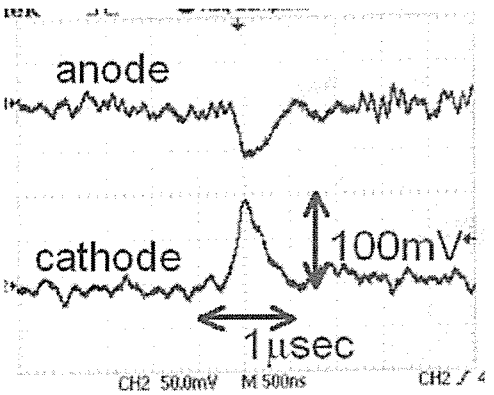

Fig. 5. The first signal of the new μ-PIC by the β-rays from ^{90}Sr/Y. The gas is argon 90% and ethane 10%, and the anode voltage is 500 V.

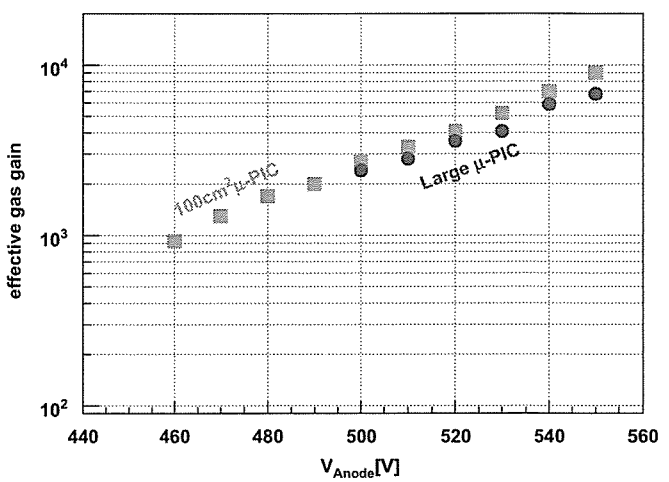

Fig. 6. The effective gas gain of the new μ-PIC, in comparison to the previous μ-PIC. The gas is argon 90% and ethane 10%.

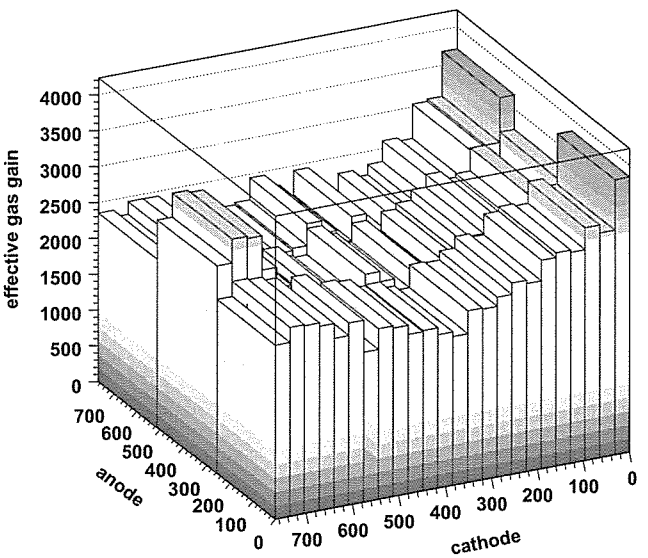

Fig. 7. The effective gas gain map of the new μ-PIC. The gas is argon 90% and ethane 10%, and the anode voltage is 500 V. The bad pixels concentrate in the area of which the cathode number is between 0 and 100 in this figure.

of the bad pixels are shown by the cross in Fig. 4(c). The bad pixels concentrate at the opposite side of the dead pixel area. In comparison to the distribution of the dead pixels, the bad pixels distribute at random in the whole area, although the number is very little (~0.02% in the whole area). For the stable operation, we are improving the production process with TOSHIBA.

3. The performance for X-rays

The new μ-PIC has 1536 readout strip electrodes (786 anode + 768 cathode), and each strip is read out by the